Supplementary Information

Synergistic strain and N-doping for creating physical orientation selectivity in chemical etching of graphene nanoribbons

Xiangyu Meng,[ae] Yuansen Zhu,[be] Ying Li,[b] Chengqian Huang,[a] Shiming Zhou,[*c] Kuibo Yin,[d] Liang Ma,[*b] Jinlan Wang,[b] Yueming Sun[a] and Yunqian Dai[*a]

[a]School of Chemistry and Chemical Engineering, Southeast University, Nanjing, Jiangsu 211189, China.

[b]Key Laboratory of Quantum Materials and Devices of Ministry of Education, School of Physics, Southeast University, Nanjing, Jiangsu 211189, China.

[c]Hefei National Laboratory for Physics Sciences at the Microscale, University of Science and Technology of China, Hefei, Anhui 230026, China.

[d]SEU-FEI Nano-Pico Center, Key Laboratory of MEMS of Ministry of Education, Southeast University, Nanjing, Jiangsu 210096, China.

[e]These authors contributed equally: Xiangyu Meng and Yuansen Zhu.

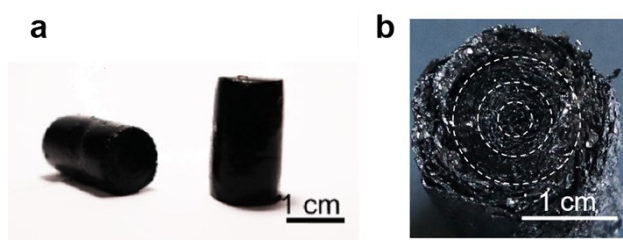* Correspondence: daiy@seu.edu.cn; zhousm@ustc.edu.cn; liang.ma@seu.edu.cn

Fig. S1 The optical image of cylindrical N-RGO hydrogel (**a**) before and (**b**) after aqueous removal, with circles for highlighting the ring-by-ring structures in (**b**).
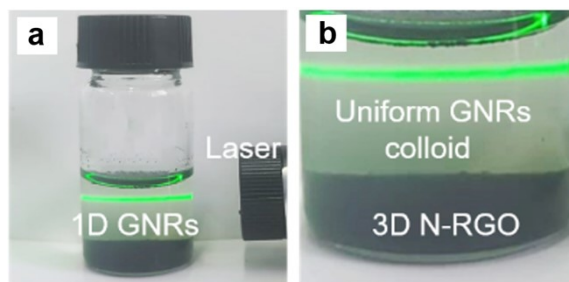
Fig. S2 (a) Optical image of N-GNRs (top layer, light yellow color) and N-RGO (bottom layer, black color); **(b)** Tyndall effect can be observed in the uniform N-GNRs colloid.
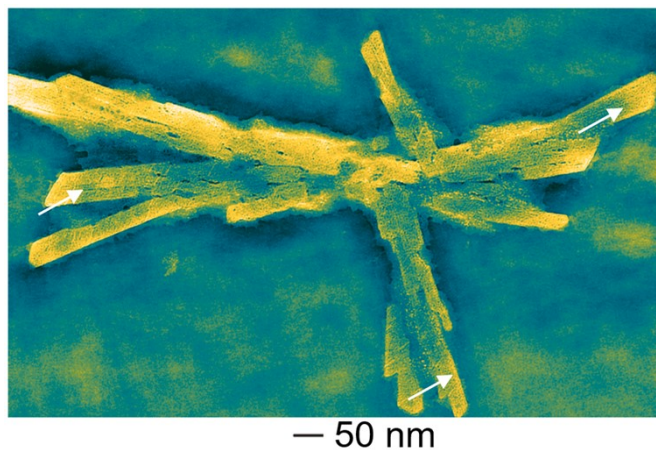
— 50 nm

Fig. S3 TEM image of the dispersed N-GNRs produced in a 25 mL-cylindric hydrothermal reactor. The arrows highlight the nanoribbons.
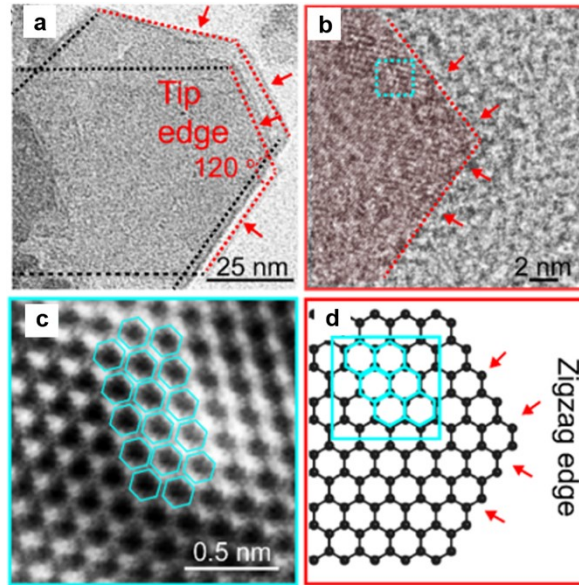
Fig. S4 (**a**) TEM image and (**b**) the magnified view for showing the N-GNRs with tip-like short edges (highlighted by red lines and arrows); (**c**) The FFTs and (**d**) schematic illustrations of zigzag carbon chains on short edges.
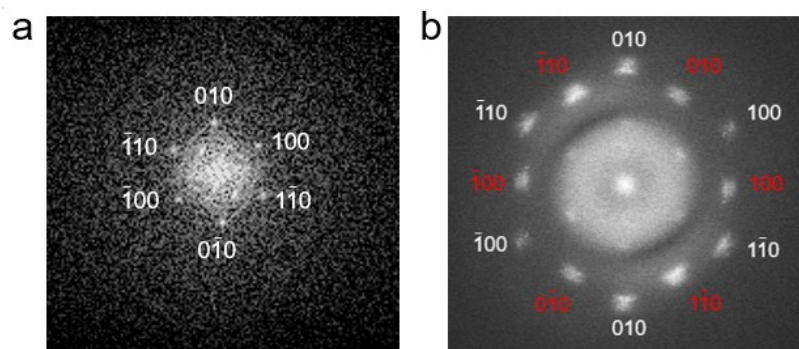
Fig. S5 Selected area electron diffraction (SAED) patterns obtained from the GNRs' edges with the (**a**) single-layer graphene pattern and the (**b**) few-layer graphene pattern.
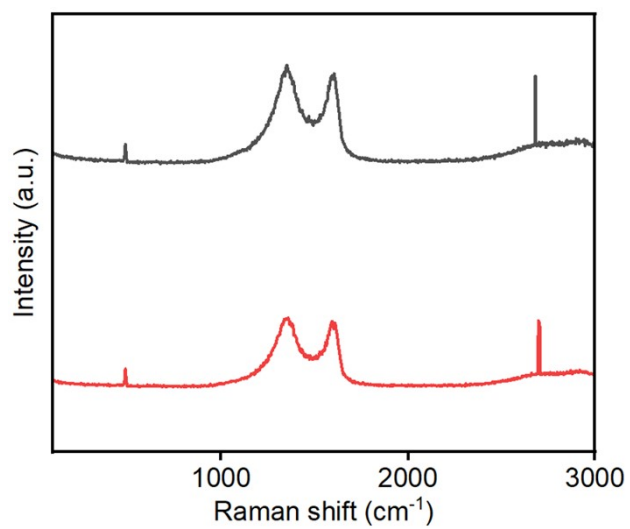
Fig. S6 Raman spectra of GO (black curve) and GNRs (red curve).

Note S1. The Raman analysis of GO and GNRs.

We have further analyzed the disordering degree of GO and the reduced graphene nanoribbons (rGNRs) by supplementing our study with Raman spectroscopy (Fig. S6). The Raman characterization of GO and rGNRs was conducted to evaluate the number of layers and defect levels. The results show that the intensity ratio of the D peak to the G peak (I_D/I_G) for the GO used in our synthesis was 1.03, indicating a moderate level of defects due to oxygen-containing functional groups, which enhances its reactivity for cutting reactions. The defects in GO play a critical role in determining the cutting pathways. As shown in Fig. 2, the starting points for nanoribbon cutting are precisely those point defects or vacancies, which may also serve as nucleation sites for nitrogen doping. The introduction of nitrogen atoms, having a larger spatial volume than the original carbon atoms, further facilitates the cutting process of nanoribbons by creating additional strain.

After cutting and reduction, the I_D/I_G ratio of the resulting rGNRs decreased to 1.007, reflecting partial restoration of the sp^2 carbon framework, the reduction process effectively repaired some defects in the material. The presence of a pronounced and symmetric 2D peak with the intensity ratio of the 2D peak to the G peak intensity ratio at ~1, further confirmed that the both GO and rGNRs were predominantly single- or few-layer (<10) structures.

The directionality of the cutting process is guided by the stress within the reactor, as evidenced by both experimental and computational analyses presented in the main text. In our synthetic strategy, using highly oxidized and defective GO sheets as starting materials enhances the cutting reactivity compared to inert graphene, not only promotes functionalization via nitrogen doping but also facilitates uniform dispersion and cutting in solution. Compared to other cutting strategies, our method cleverly utilizes stress-induced cutting to achieve directional and ordered slicing, reducing random defects while maintaining the integrity of the nanoribbon structure. Due to both the etching and doping occurring primarily at the defect sites of the active GO, the N-doping predominantly takes place at the GNRs' edges, forming graphitic nitrogen, while the sp^2 carbon framework in the middle remains intact, ensuring that the final product retains good electrical conductivity.
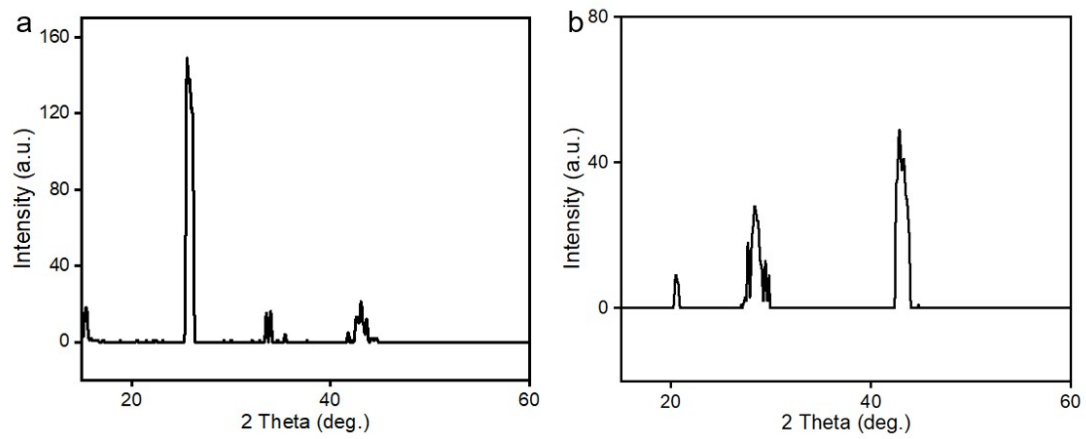
Fig. S7 XRD spectra of (**a**) GO and (**b**) N-GNRs.

Note S2. The XRD analysis of GO and GNRs before and after etching.

The XRD results (Fig. S7) show that before the reaction, GO exhibited a strong (001) peak, indicating a high degree of oxidation, while the (002) peak was weak. After the reaction, the nanoribbons displayed a significantly weakened (001) peak and an enhanced (002) peak, suggesting the removal of oxygen-containing functional groups and the partial restoration of the graphitic structure. These results clearly demonstrate that the reduction and cutting processes led to a gradual removal of sp³-hybridized oxygen functional groups and a corresponding structural transition back to the planar sp² configuration.
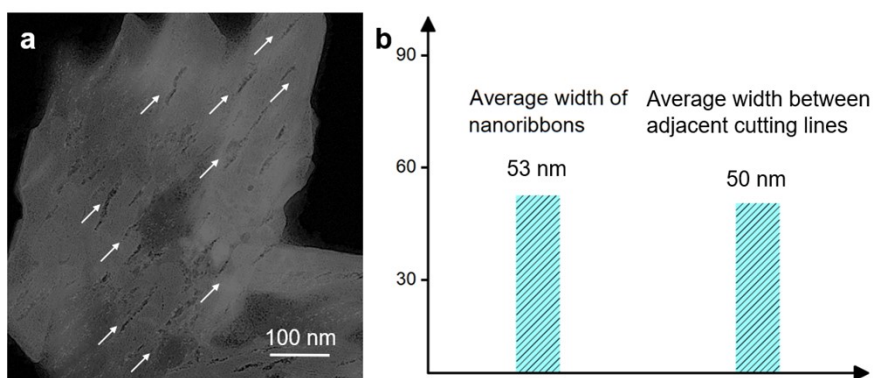
Fig. S8 (a) TEM image of a N-RGO sheet with typical aligned cutting lines after 3 h-cutting. The arrows highlight the cutting lines; **(b)** The consistency between average widths of N-GNRs and average widths among the cutting lines.
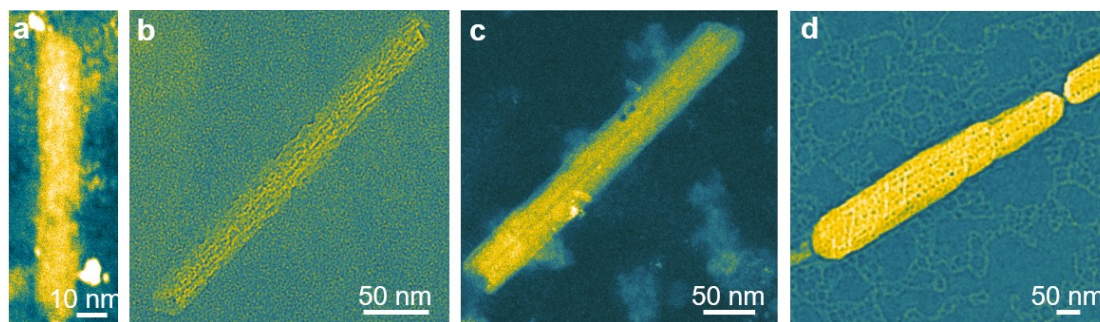
Fig. S9 TEM image of the monodispersed N-GNR shown in Fig. 4d, with increased average widths from (**a**)16 nm, (**b**) 29 nm, (**c**) 37 nm to (**d**) 103 nm, as a result of increased diameters of the cylindric hydrothermal reactors from 15 mm to 30 mm. The TEM of N-GNR with width of 50 nm was already shown in Fig. 1.
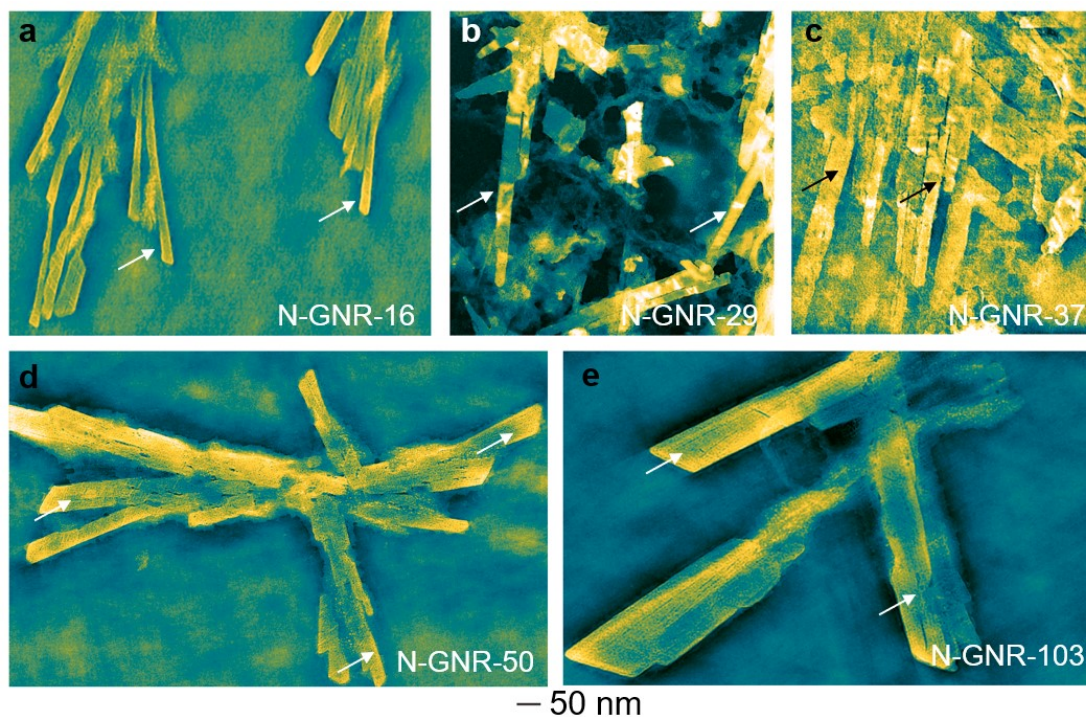
Fig. S10 TEM image of the dispersed multiple N-GNRs with increased average widths from (**a**) 16, (**b**) 29, (**c**) 37, (**d**) 50 to (**e**) 103 nm, as a result of increased diameters of the cylindric hydrothermal reactors from 15 to 30 mm. The details of sample names can be found in Methods. The arrows highlight the nanoribbons. The TEM image of N-GNR with width of 50 nm was the same one in Fig. S3, for better comparison of widths with others.

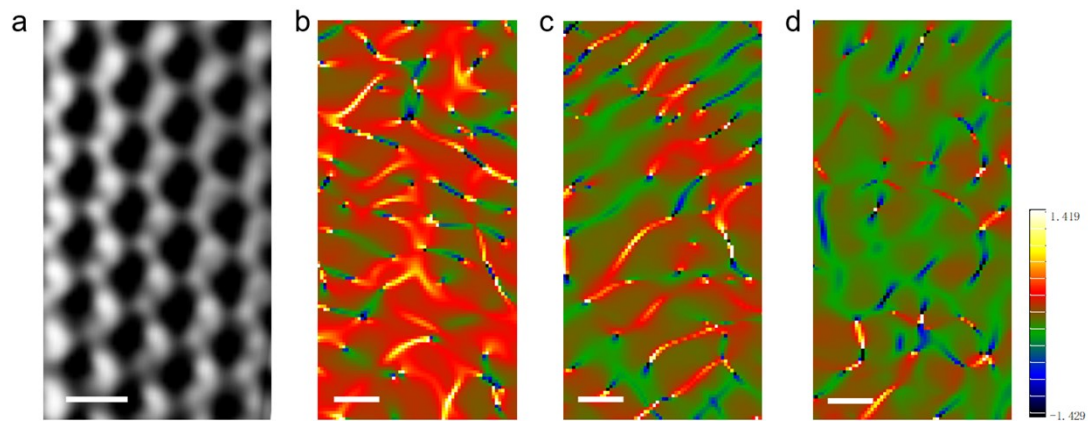**Fig. S11** (**a**) Edge structure of a GNR with an average width of 16 nm, showing a complete and relatively clear single- or few-layered six-membered ring structure. (**b-d**) GPA lattice strain visualization analysis results of GNRs with average widths of 16 nm, 50 nm, and 103 nm, respectively. The right legend shows the color-to-stress magnitude correlation. The scale bar in (**a**) and (**b**) was 0.15 nm.
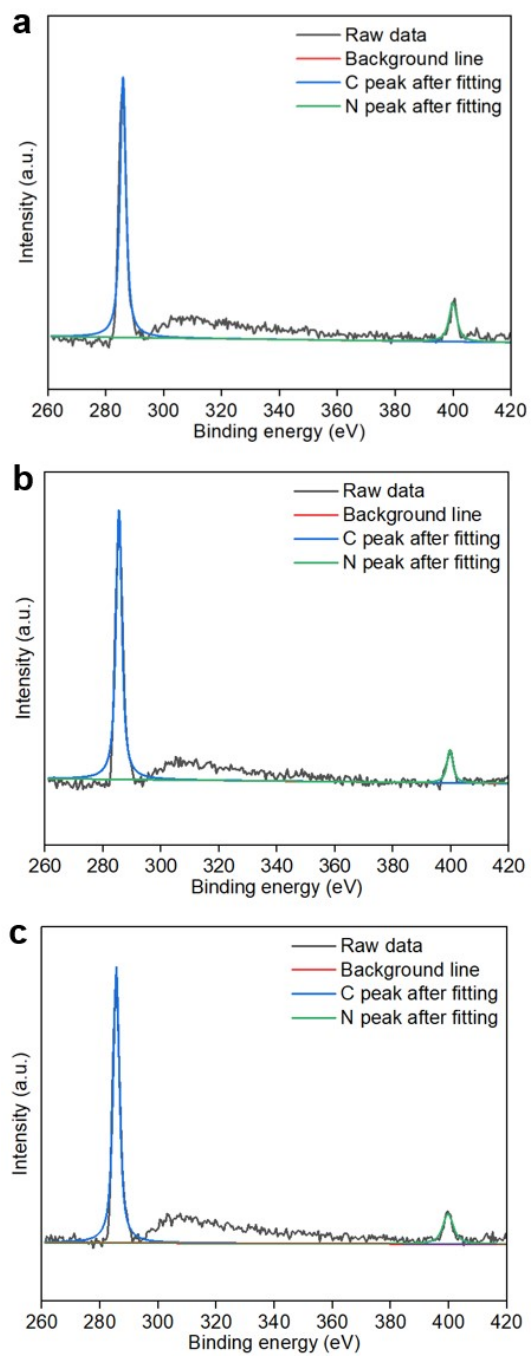
Fig. S12 N 1*s* and C 1*s* XPS survey spectra of N-GNRs with widths of (**a**)16, (**b**) 50 and (**c**) 103 nm.
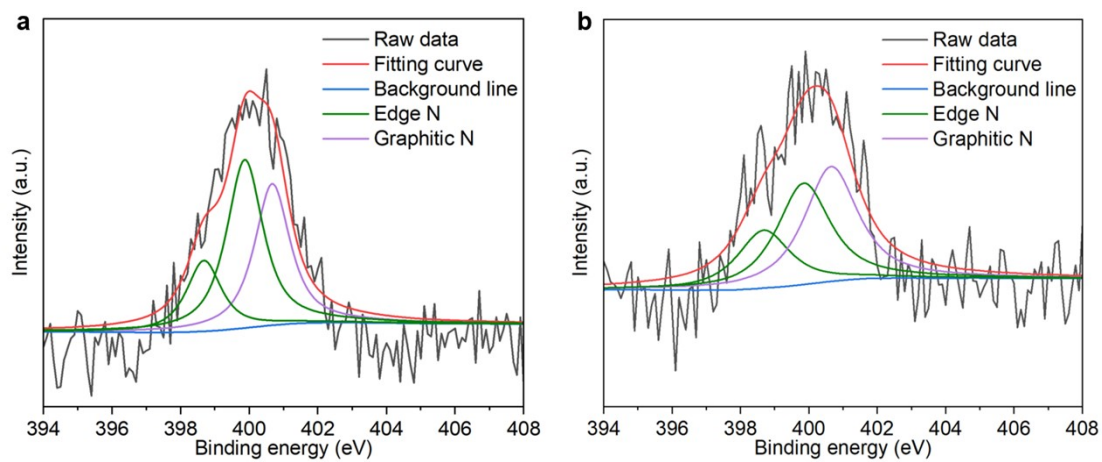
Fig. S13 N 1*s* XPS survey spectra of N-GNRs with widths of (**a**)16 and (**b**) 103 nm. The N1*s* XPS survey spectra of N-GNRs with widths of 50 nm can be found in Fig. 2b in main text.
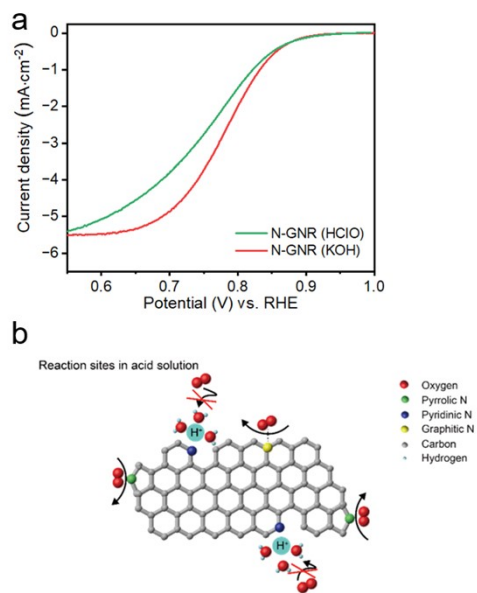
Fig. S14 (a) ORR LSV curves of N-GNRs in acidic and alkaline electrolytes. **(b)** Schematic illustration explaining the preservation of active sites in N-GNRs under acidic electrolyte conditions.

Fig. S15 (**a**) ORR LSV curves of N-GNRs under full-spectrum (300–2500 nm) light irradiation. (**b**) Photothermal imaging temperature distribution of inks with and without N-GNRs under the same light irradiation conditions.

Fig. S16 The electron transfer-number and peroxide percentage of N-GNRs in KOH.

Fig. S17 The stability tests of N-GNRs in KOH.

Table S1 A comparison of ORR electrocatalysis performance among this work and recent advanced reports.

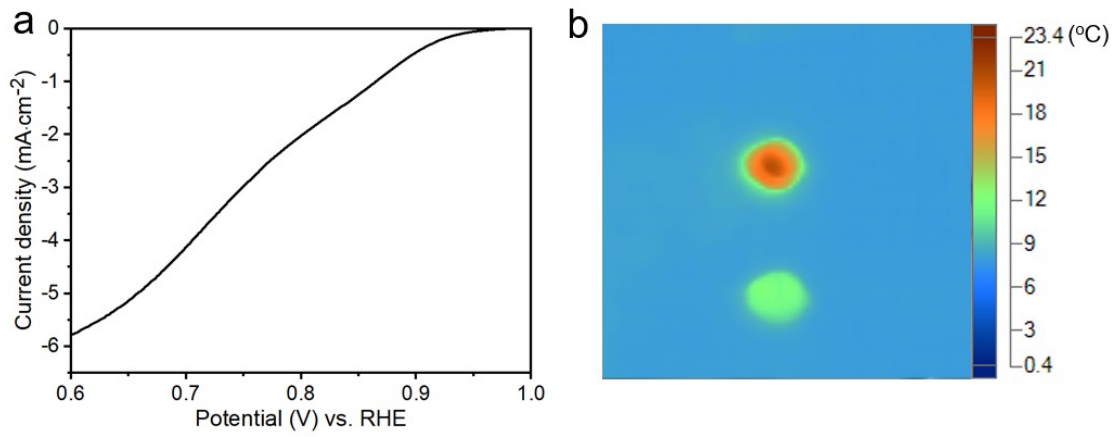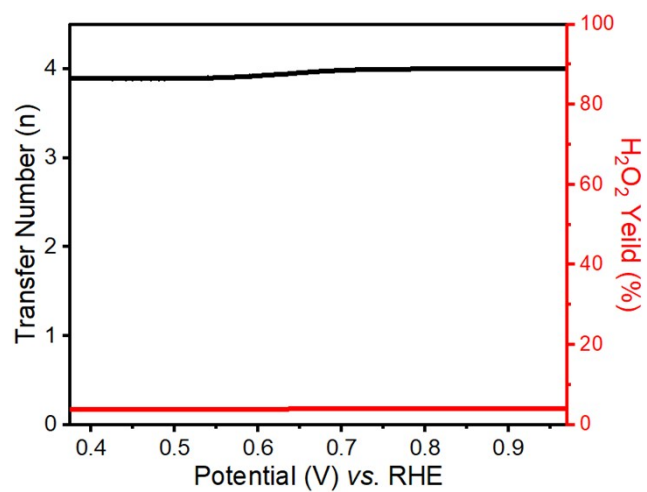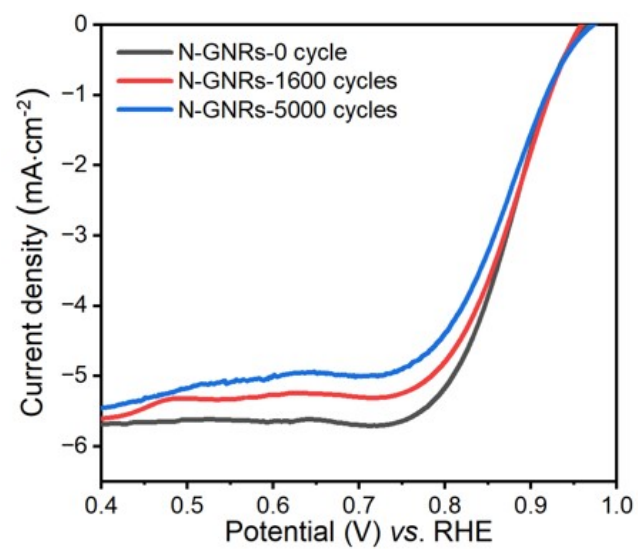| Materials	Onset potential (V *vs.* RHE)	Mass activity (mA·mg^{-1})	Selectivity for H$_2$O (%)	Shift on half-wave potential (mV) after cycling	Conditions	Reference
N-GNR-50	0.92	582	96.3	0.009, 5000 cycles	Alkaline	This work
N-GNR-16	0.93	760			Alkaline	This work
NC	0.79	19.6			Alkaline	Nat. Sustain., 2023[1]
FeCo-NC	0.89	18.8			Alkaline	Nat. Commun., 2023[2]
Co/CNT	0.85	6.0			Alkaline	Nat. Commun., 2023[3]
N-CF	0.77	150			Alkaline	Nat. Commun., 2023[4]
Rh/NC	0.82	62.0			Alkaline	Nat. Commun., 2022[5]
B-doped Carbon	0.77	35.0			Alkaline	Nat. Commun., 2021[6]
Cu/NG	0.91	170			Alkaline	Nat. Commun., 2021[7]
HLM-C	0.90	46.7			Alkaline	Nat. Commun., 2021[8]
HESAC	0.92	6.20			Alkaline	Nat. Commun., 2022[9]
Pt/C	0.85	300			Alkaline	Adv. Funct. Mater., 2022[10]
N/C-Br	0.90	156			Alkaline	Adv. Funct. Mater., 2022[11]
Fe-N-C	0.89	11.9			Alkaline	Adv. Funct. Mater., 2022[12]
Co$_3$O$_4$	0.70	500			Alkaline	ACS Nano, 2022[13]
Pt/C and A-silicalite-1-NCs	0.90	214			Buffer (pH	Nat. Catal. 2023[14]

|						
Graphene	0.88	37			Alkaline	Adv. Funct. Mater., 2024[15]
Graphene quantum dots	0.80	4.3			Alkaline	Adv. Mater., 2023[16]
Cobalt phthalocyanine complexes			80		Acid	Angew. Chem. Int. Ed., 2024[17]
Pt			76.7		Acid	Nat. Commun., 2022[18]
F-doped carbon-supported Pt				5, 5000 cycles	Acid	Angew. Chem. Int. Ed., 2024[19]
$Fe_2–S_1N_5/SNC$				26, 5000 cycles	Acid	Energy Environ. Sci., 2024[20]
Fe-Zn@SNC				25, 5000 cycles	Acid	Angew. Chem. Int. Ed., 2023[21]
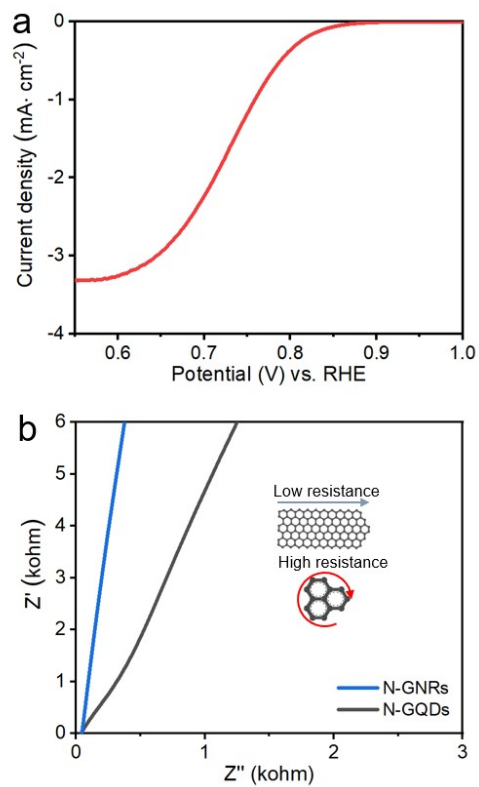
Fig. S18 (**a**) ORR LSV curves of nitrogen-doped graphene quantum dots (N-GQDs). (**b**) EIS performance comparison between N-GQDs and N-GNRs, with the inset illustrating how the one-dimensional structure of N-GNRs facilitates efficient electron transport.

Note S3. Comparing the ORR electrochemical performance of nitrogen-doped graphene quantum dots and nitrogen-doped nanoribbons synthesized in the same batch to analyze the dimensional advantages.

To highlight the advantages of the nanoribbons' one-dimensional structure, we compared their performance with zero-dimensional quantum dots synthesized in the same batch. LSV and EIS results demonstrated the superiority of the nanoribbons, which exhibited a higher onset potential (0.920 V) compared to quantum dots (0.855 V), and a greater current density (5.77 mA/cm² *vs*. 3.31 mA/cm² (Fig. S18a). Additionally, the nanoribbons showed lower interface resistance (61 Ω *vs*. 97 Ω, Fig. S18b). These findings confirm that the nanoribbons' extended conductive pathways and higher density of exposed active sites significantly enhance their catalytic performance compared to quantum dots.
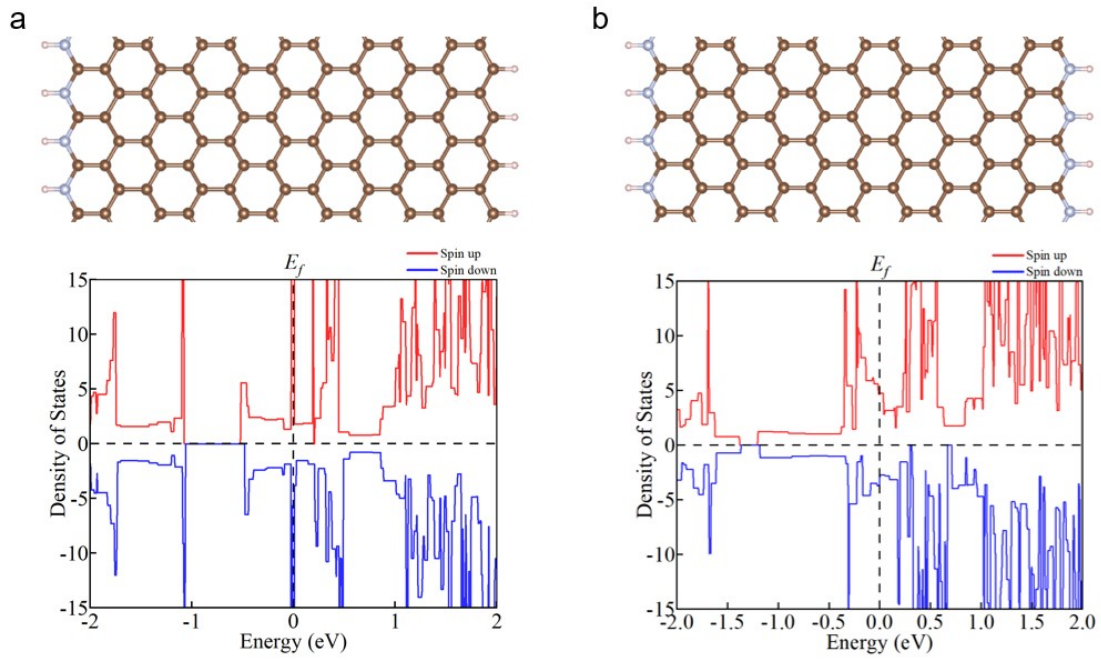
Fig. S19 (a) Top: Model of single-edge N-GNRs; Bottom: DOS results of the corresponding structure. **(b)** Top: Model of double-edge N-GNRs; Bottom: DOS results of the corresponding structure.
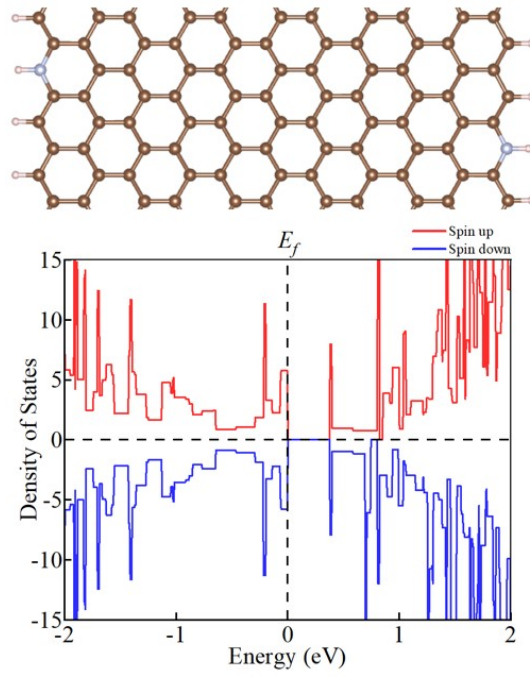
Fig. S20 Top: Model of double-edge N-GNRs with low doping concentration; Bottom: DOS results of the corresponding structure.

Fig. S21 (a) Gibbs free energy calculation model for the process of oxygen adsorption to oxygen dissociation (O-O*) on zigzag-edged N-GNRs. **(b)** Corresponding initial unit structure. **(c)** Corresponding final unit structure.

Fig. S22 (**a**) Gibbs free energy calculation model for the process of oxygen adsorption to oxygen dissociation (O-O*) on armchair-edged N-GNRs. (**b**) Corresponding initial unit structure. (**c**) Corresponding final unit structure.

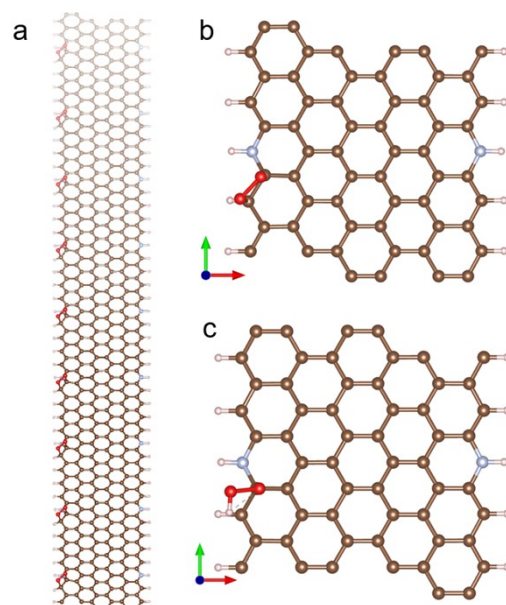**Fig. S23** (**a**) Gibbs free energy calculation model for the process of oxygen adsorption to oxygen dissociation (O-O*) on wider zigzag-edged N-GNRs. (**b**) Corresponding initial unit structure. (**c**) Corresponding final unit structure.
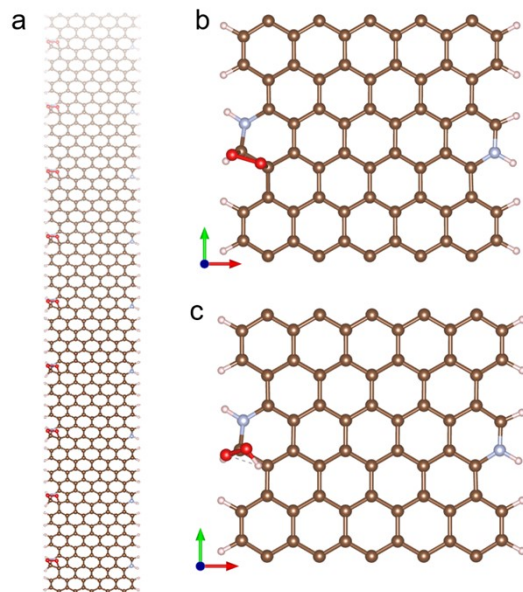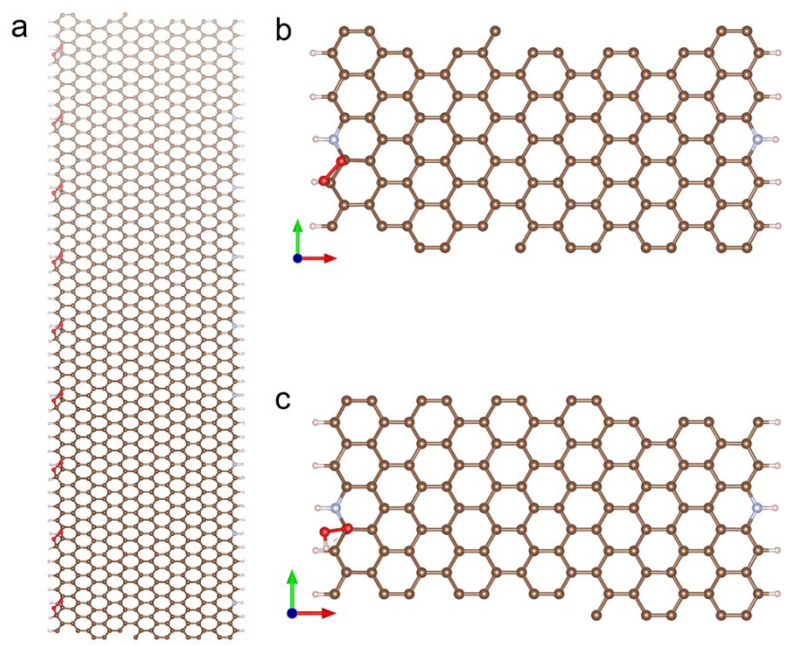
Note S4. Analyzing the relationship between electrocatalytic ORR performance and N-GNR structures based on DFT calculations.

DFT calculations analyzed the influence of edge and doping structures on the bandgap of N-GNRs and their correlation with conductivity in electrochemical reactions (Fig. S19 and 20). The results show that N-GNRs with dual-side N-doping exhibit significantly smaller bandgaps compared to single-side doping (*i.e.*, 0.175 eV for dual-side *vs*. 0.555 eV for single-side doping under the electric field of 0.5 V/Å). Additionally, we found that higher N-doping concentrations (close to the experimental values) further reduce the bandgap (0.175 eV for high concentration *vs*. 0.376 eV for low concentration). This reduced bandgap enhances the N-GNR's conductivity, which directly benefits electron transfer during catalytic reactions.

Furthermore, we investigated the changes in Gibbs free energy (ΔG) for O_2 adsorption and dissociation (O_2 to O-O*) during the electrochemical ORR (Fig. S21-23), for elucidating the relationship between structural features and ORR catalytic activity. In dual-side N-doped GNRs, zigzag edges exhibit lower absolute ΔG values (-3.21 eV) compared to armchair edges (-5.10 eV), indicating that zigzag edges are more favorable for the ORR. For zigzag-edged N-GNRs, narrower ribbons show lower absolute ΔG values (-3.21 eV for narrower ribbons *vs*. -3.35 eV for wider ribbons), suggesting that narrower zigzag-edged N-GNRs are more active ORR catalysts. This conclusion is consistent with experimental findings that narrower zigzag-edged N-GNRs exhibit higher current densities and lower overpotentials in ORR tests shown in Fig. 5c and d.
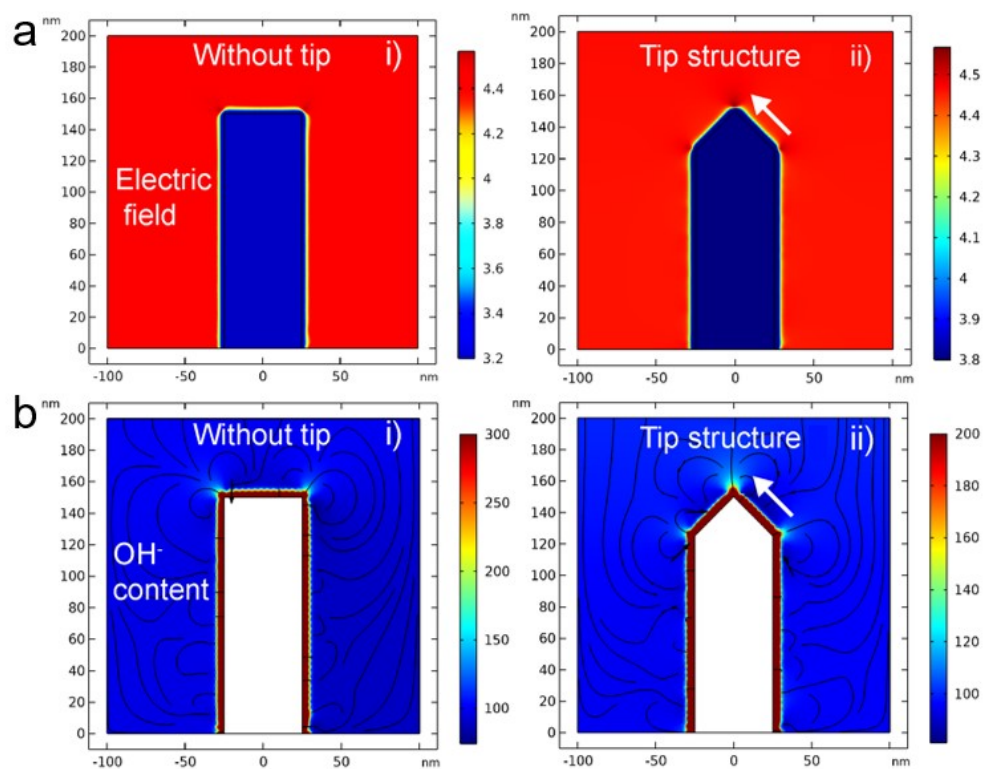
Fig. S24 (a) Comparison of charge density between the conventional short-edge structure (i) and (ii) the GNR-tip short-edge structure. **(b)** Comparison of hydroxide ion enrichment concentration between the conventional short-edge structure (i) and (ii) the GNR-tip short-edge structure. Arrows highlighted the concentration area.

Note S5. Analyzing the advantageous role of the unique GNR-tip short-edge in ORR electrochemical reactions based on FEA results.

FEA simulations were further employed to explore the structure-activity relationship and design of the short edge of N-GNRs at a nanometer scale. Two models of N-GNRs were built for comparisons, involving the nanoribbon without (i) and with tip-structure (ii). Simulation suggests that a remarkably enhanced local electrostatic field can be generated on tip-edges (highlighted by the arrows) with the locally concentrated positive charges. During the electron-concentration, the electrostatic repulsion drives the migration of free electrons to the regions of the sharpest curvature on the negatively charged tips, potentially enhancing the current density with a 15% improvement (Fig. S24). Then, a Gouy-Chapman-Stern model in FEA simulation was used to map the surface adsorbed OH^- ion density on tip-edges of N-GNRs (Fig. S24). Notably, under the locally enhanced electrostatic field, a remarkable increase in surface-adsorbed OH^- ion concentration (highlighted by the arrows for indicating mass-transfer directions) was observed at the N-GNRs' tips. It is known that, OH^- ions are the important species in the reaction steps of the ORR in alkaline solution, which act as a precursor for dissociative adsorption of molecular oxygen, chemisorption of reaction intermediate and catalyzing the $4e^-$ reduction of O_2. Hence, the aggregation of OH^- ions at the tips can lead to a further increase of reduction current in ORR process. It demonstrated tip-edge nanostructure design of N-GNRs offers an attractive solution on easily concentrating electrolyte anions on the active O_2 reduction sites by the local high electric fields. These results further confirm the great potential of our assumed design of N-GNRs can easily accelerate ORR under the lower applied overpotential with lower resistance and high mass activities.
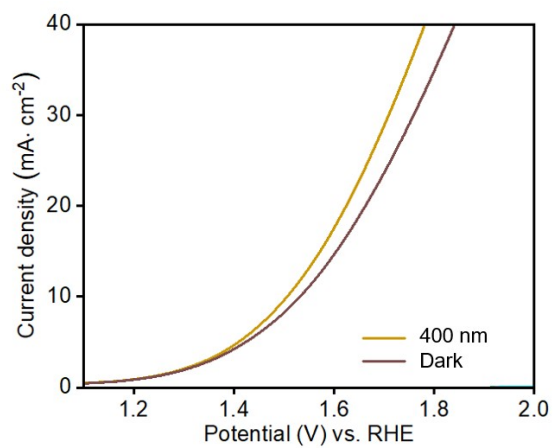
Fig. S25 OER LSV curves performed by N-GNRs under light or dark conditions.

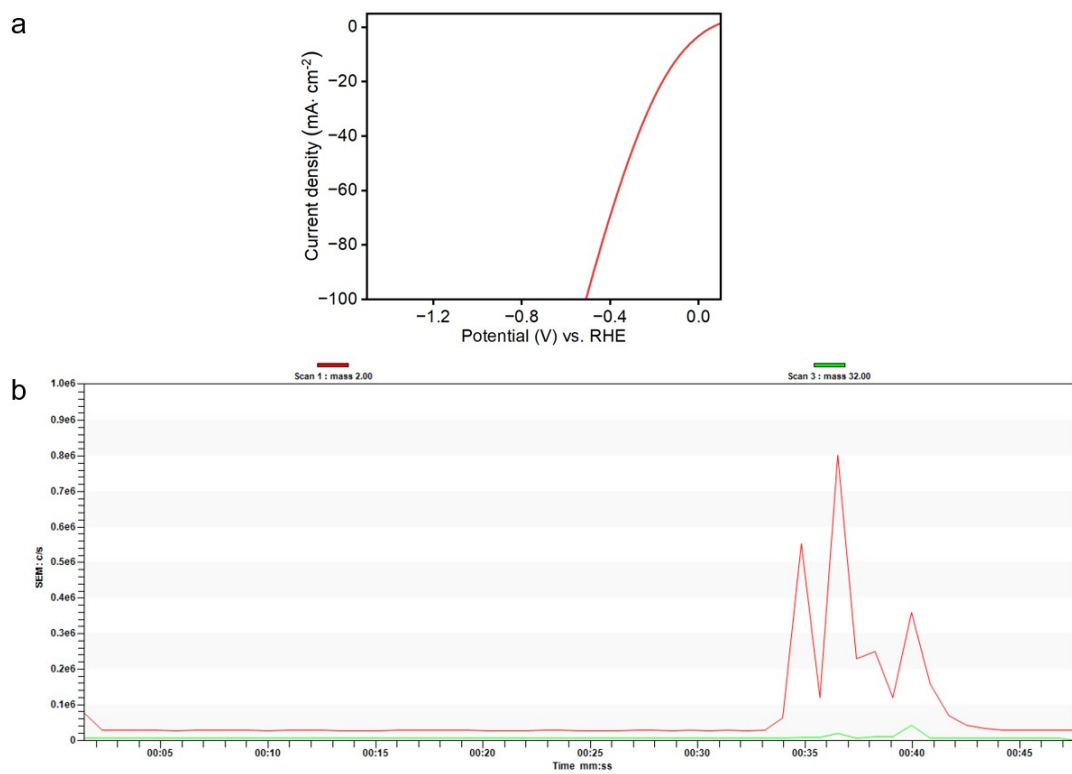**Fig. S26** (**a**) HER LSV curve of N-GNRs, showing the electrochemical performance for hydrogen evolution reaction. (**b**) DEMS curve showing the hydrogen production rate of N-GNRs under HER conditions, recorded in real-time during the reaction.

Table S2. A comparison of OER and HER electrocatalysis performance among this work and recent advanced reports.

Materials	Over potential (mV *vs*. RHE)	Reference
N-GNR-50	300 for OER; 76 for HER	This work
Co-Graphene	370 for OER	Angew. Chem. Int. Ed., 2024[22]
NiFe	316 for OER	Small, 2023[23]
n-Si/TiO$_2$/NiO$_x$/Gr	382 for OER	Adv. Mater., 2023[24]
Graphene	648 for OER	Adv. Funct. Mater., 2024[15]
RuxPty@rGO	91.4 for HER	Adv. Funct. Mater., 2024[25]
Co$_3$S$_4$/MoS$_2$	220 for HER	Adv. Sci., 2024[26]

Table S3. The AFM measurement results of GO sheets.

Horizontal Distance (μm)	Vertical Distance (nm)	Surface Distance (μm)	Angle	R_{max}	R_z	R_z Count	R_{ms}	R_a (Frequency Cutoff) (nm)
0.298	0.707	0.298	0.1	0.8	0	0	0.06	0.304
0.227	1.109	0.227	0.2	1.24	0	0	0.05	0.179
0	0	0	0	0	0	0	0	0

Horizontal Distance (μm) means the horizontal span measured on the sample surface.

Vertical Distance (nm) represents the thickness of the graphene layer, indicating the height difference measured using AFM.

Surface Distance (μm) means the surface path length measured between two points on the sample.

Angle represents the inclination angle of the measurement region, often related to the surface morphology.

R_{max} means the maximum roughness, indicating the largest height difference within the test region.

R_z represents the ten-point height average roughness, calculated as the mean difference between the five highest peaks and the five lowest valleys on the surface.

R_z Count means the number of occurrences of roughness within a specific height range.

R_{ms} represents the Root Mean Square Roughness, indicating the overall roughness by the root mean square of surface height deviations.

R_a (Frequency Cutoff) (nm) means the arithmetic average roughness, calculated as the mean of the absolute values of the surface height deviations, with high-frequency noise potentially filtered out.

Notes and references

1. X. Lei, Q. Tang, Y. Zheng, P. Kidkhunthod, X. Zhou, B. Ji and Y. Tang, *Nat. Sustain.*, 2023, **6**, 816.

2. Z. Jiang, X. Liu, X. Liu, S. Huang, Y. Liu, Z. Yao, Y. Zhang, Q. Zhang, L. Gu, L. Zheng, L. Li, J. Zhang, Y. Fan, T. Tang, Z. Zhuang and J. Hu, *Nat. Commun.*, 2023, **14**, 1822.

3. W. Fan, Z. Duan, W. Liu, R. Mehmood, J. Qu, Y. Cao, X. Guo, J. Zhong and F. Zhang, *Nat. Commun.*, 2023, **14**, 1426.

4. M. Yan, Z. Wei, Z. Gong, B. Johannessen, G. Ye, G. He, J. Liu, S. Zhao, C. Cui and H. Fei, *Nat. Commun.*, 2023, **14**, 368.

5. J. Chen, Q. Ma, X. Zheng, Y. Fang, J. Wang and S. Dong, *Nat. Commun.*, 2022, **13**, 2808.

6. Y. Xia, X. Zhao, C. Xia, Z. Wu, P. Zhu, J. Y. Kim, X. Bai, G. Gao, Y. Hu, J. Zhong, Y. Liu and H. Wang, *Nat. Commun.*, 2021, **12**, 4225.

7. G. Han, X. Zhang, W. Liu, Q. Zhang, Z. Wang, J. Cheng, T. Yao, L. Gu, C. Du, Y. Gao and G. Yin, *Nat. Commun.*, 2021, **12**, 6335.

8. X. Zhong, M. Oubla, X. Wang, Y. Huang, H. Zeng, S. Wang, K. Liu, J. Zhou, L. He, H. Zhong, Alonso-Vante, H. Wang, C. Wu, H. Lin, C. Chen, Z. Hu, Y. Huang and J. Ma, *Nat. Commun.*, 2021, **12**, 3136.

9. P. Rao, Y. Deng, W. Fan, J. Luo, P. Deng, J. Li, Y. Shen and X. Tian, *Nat. Commun.*, 2022, **13**, 5071.

10. C. Xin, W. Shang, J. Hu, C. Zhu, J. Guo, J. Zhang, H. Dong, W. Liu and Y. Shi, *Adv. Funct. Mater.*, 2022, **32**, 2108345.

11. G. Ye, S. Liu, K. Huang, S. Wang, K. Zhao, W. Zhu, Y. Su, J. Wang and Z. He, *Adv. Funct. Mater.*, 2022, **32**, 2111396.

12. Y. Yuan, Q. Zhang, L. Yang, L. Wang, W. Shi, P. Liu, R. Gao, L. Zheng, Z. Chen and Z. Bai, *Adv. Funct. Mater.*, 2022, **32**, 2206081.

13. G. K. K. Gunasooriya, M. E. Kreider, Y. Liu, J. Z. Z. Zeledon, Z. Wang, E. Valle, A. Yang, A. Gallo, R. Sinclair, M. Stevens, T. Jaramillo and J. N. Gunasooriya, *ACS Nano*, 2022, **16**, 6334–6348.

14. A. E. Thorarinsdottir, D. P. Erdosy, C. Costentin, J. A. Mason and D. Nocera, *Nat. Catal.*, 2023, **6**, 425–434.

15. M. Yu, F. Guo, L. Xu, Y. Zhang, W. Ni, J. Wang, Y. Wei, X. Chen, J. Yang, H. Li, J. Wang, and J. Wang, *Adv. Funct. Mater.*, 2024, 202411935. https://doi.org/10.1002/adfm.202411935

16. M. Fan, Z. Wang, K. Sun, A. Wang, Y. Zhao, Q. Yuan, R. Wang, J. Raj, J. Wu, J. Jiang and L. Wang, *Adv. Mater.*, 2023, **35**, 2209086.

17. A. R. Kottaichamy, M. A. Nazrulla, M. Parmar, R. Thimmappa, M. C. Devendrachari, C. P. Vinod, M. Volokh, H. M. N. Kotresh, M. Shalom and M. O. Thotiyl, *Angew. Chem. Int. Ed.*, 2024, **63**, e202405664.

18. J. Zhao, C. Fu, K. Ye, Z. Liang, F. Jiang, S. Shen, X. Zhao, L. Ma, Z. Shadike, X. Wang, J. Zhang and K. Jiang, *Nat. Commun.*, 2022, **13**, 685.

19. J. Liang, L. Liang, B. Zeng, B. Feng, L. Du, X. Qiu, Y. Wang, H. Song, S. Liao, M. Shao and Z. Cui, *Angew. Chem. Int. Ed.*, 2024, **63**, e202412825.

20. Y. Li, X. Luo, Z. Wei, F. Zhang, Z. Sun, Z. Deng, Z. Zhan, C. Zhao, Q. Sun, L. Zhang, W. Chen, S. Li and S. Pang, *Energy Environ. Sci.*, 2024, **17**, 4646.

21. Y. Xie, X. Chen, K. Sun, J. Zhang, W. H. Lai, H. Liu and G. Wang, *Angew. Chem. Int. Ed.*, 2023, **135**, e202301833.

22. J. Yang, G. Dai, W. Song, P. E. P. Win, J. Wang and X. Wang, *Angew. Chem. Int. Ed.* 2024, e202416274. https://doi.org/10.1002/anie.202416274.

23. Z. Lyu, S. Yu, M. Wang, P. Tieu, J. Zhou, Q. Shi, D. Du, Z. Feng, X. Pan, H. Lin, S. Ding, Q. Zhang and Y. Lin, *Small* 2024, **20**, 2308278.

24. G. Xie, X. Liu, B. Guo, T. Tan, and J. R. Gong, *Adv. Mater.*, 2023, **36**, 202211008.

25. J. Yang, J. Feng, Y. Cao, Y. Xiao, L. Qiao, K. An, J. Yang, J. Peng, H. Pan and H. M. Cheng, *Adv. Funct. Mater.*, 2024, 202411081. https://doi.org/10.1002/adfm.202411081

26. D. W. Kim, J. Kim, J. H. Choi, D. H. Jung, and J. K. Kang, *Adv. Sci.*, 2024, **11**, 202408869.
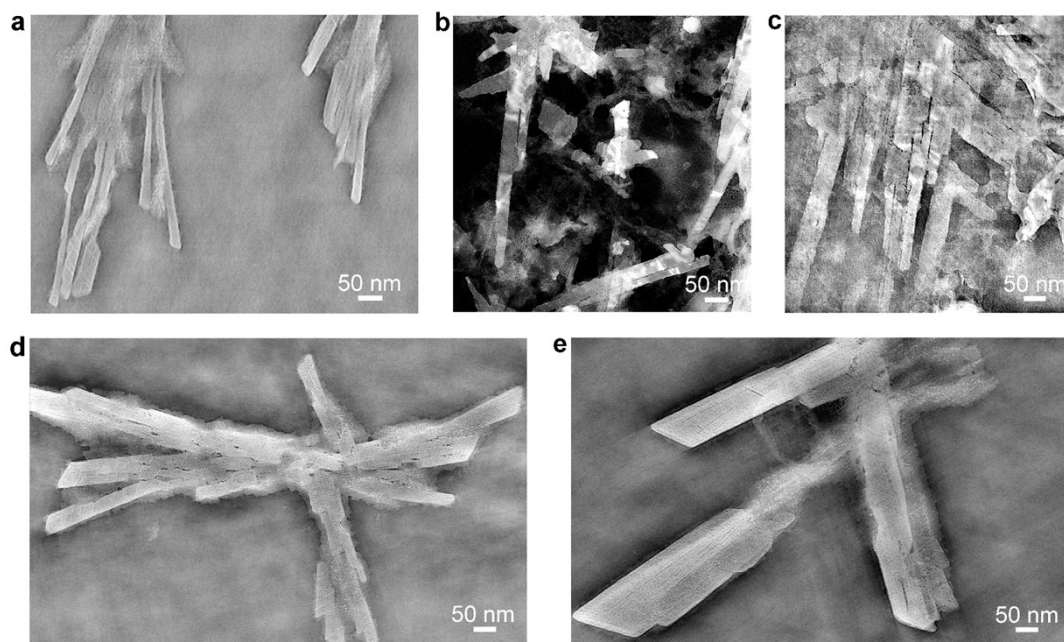
Extended Data Fig. 1-3: The pristine TEM images for GNRs shown in the Fig. 1b, Fig. 2c, Fig.3 a-c, Fig. 4d, Fig. S3, Fig. S6 and S7, without changing the color map.
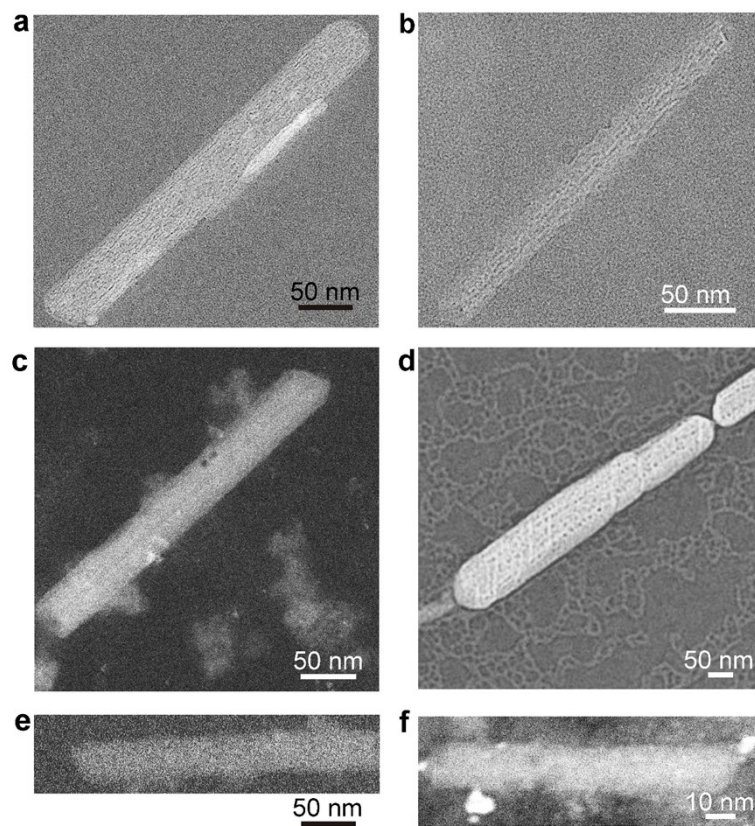
Extended Data Fig. 1 The pristine TEM images in the (**a**) Fig. 1b and Fig. 4d, (**b**) Fig. S6b and Fig. S4d, (**c**) Fig. S6c and Fig. S4d, (**d**) Fig. S6d and Fig. 4d, (**e**) Fig. 2c, (**f**) Fig. S6a and Fig. 4d.

250 nm   10 nm   50 nm
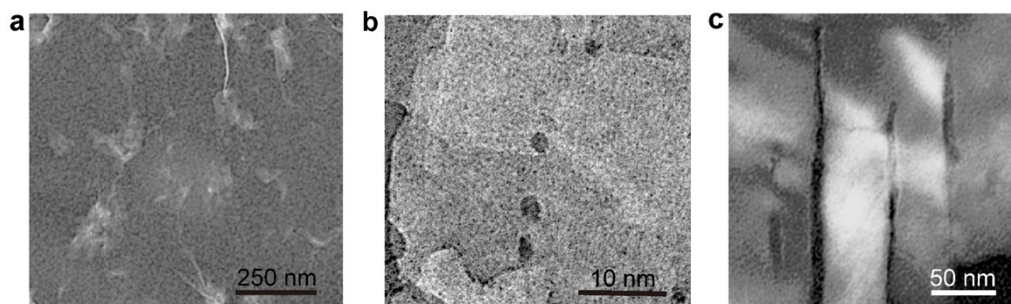
Extended Data Fig. 2 The pristine TEM images in the (**a**) Fig. 2a, (**b**) Fig. 2b, (**c**) Fig. 2c.

Extended Data Fig. 3 The pristine TEM images in the (**a**) Fig. S7a, (**b**) Fig. S7b, (**c**) Fig. S7c, (**d**) Fig. S3 and Fig. S7d, (**e**) Fig. S7e.